

**Experimental Visualization of Commercial Lithium Ion Battery Cathodes:
Distinguishing Between the Microstructure Components Using Atomic Force
Microscopy**

J.S. Terreblanche ^a, D.L. Thompson ^a, I.M. Aldous ^b, J. Hartley ^a,

A.P. Abbott ^a, and K.S. Ryder ^a

^a Materials Centre, Department of Chemistry, University of Leicester, Leicester,
LE1 7RH, UK.

^b Future Manufacturing Research Institute, College of Engineering, Swansea
University, Fabian Way, SA1 8EN, UK

* Corresponding author email: k.s.ryder@leicester.ac.uk

Abstract

The integration of lithium-ion batteries (LIB) into transport, through the implementation of hybrid and electric vehicles, is driving fundamental research into improving their performance and lifetime. The rapid production of new electric vehicles by several popular brands also raises the question of how much material will eventually need to be reused or recycled. By combining enhanced fundamental analysis of commercially utilized electrodes with fundamental chemical knowledge, answers to the scientific materials challenges of lithium ion batteries will aid in not only the implementation of battery powered electrical transport, but also the development of end of life recycling processes. Here, using quantitative nanomechanical and conductive atomic force microscopy, which are non-destructive and rapid techniques, the different components of the composite electrode are unveiled at the nanoscale, identifying the mechanism by which the active material binds together, and how the conductive network is formed. Changes in the polymer binder network are observed in an aged cell and are shown to affect the mechanical integrity of the electrode structure, which can lead to the failure of the electrode. The links between the nanomechanical and macro-mechanical properties have been evaluated using a scratch test and optical microscopy to show that the mechanical integrity of the aged cell was weaker than that of the un-touched cell.

1.0 Introduction

Lithium-ion batteries (LIB) are the favored choice for many electronic applications such as portable electronics, electric vehicles and grid storage, this is mainly due to their high operating voltages and energy densities (100 - 250 Wh/kg). In recent years, the shift from internal combustion engine (ICE) vehicles to hybrid and electric vehicles (HEV and EV) has increased significantly. Hindrance to mass integration of EVs into the market include consumer concerns such as range, power and charging time. These are dependent on the performance of the active materials within the LIB used in these devices and warrants the large research activity in this area. Understanding the degradation mechanism of LIBs as they are aged and cycled will lead to an understanding on how to increase range, performance and battery life. The development of recycling processes will also be dependent on a deeper understanding of the electrode microstructures. Previous studies into aging mechanisms focus on the degradation caused by chemical changes that occur during cycling, and how this results in permanent capacity loss. For example, solid electrolyte interphase (SEI) formation on the anode causes a permanent loss of lithium, resulting in capacity fade.^{1, 2} Solvent co-intercalation, where solvent molecules insert and intercalate into the electrode structures result in permanent defects, creating electrochemically ‘dead’ areas.³ Transition metal dissolution out of the cathode material decreases the amount of available Li insertion sites.^{4, 5} However, less attention has been paid to the degradation of the microstructures of composite electrodes. The morphology of electrode materials provides valuable information about performance characteristics. Changes in the morphology can reveal latent mechanical flaws in a material, as factors such as particle swelling and cracking can be correlated with cycling performance. This paper demonstrates the ability to image the microstructure of the composite cathode coatings in detail, at the sub-micron scale, and distinguishes between active and passive electrode components, most importantly between the metal oxide particles and the polyvinylidene fluoride (PVDF) binder

by taking advantage of their differences in hardness. Being able to image the location of the polymer binder and how it changes with cell cycling and its subsequent effect on mechanical integrity will be necessary for designing recycling processes. We have accomplished this distinction between the different electrode components using non-destructive technique known as quantitative nanomechanical mapping (QNM), this is a force mapping technique utilized by Atomic Force Microscopy (AFM). Previously in-situ scanning electron microscopy (SEM) has been utilized to show particle swelling and cracking in a SnO_2 anode material.⁶ In a related study transmission electron microscopy (TEM) has also been used for in-situ experiments that show lithium diffusion along SnO_2 nano-wires.⁷ AFM has also been used to show particle swelling and shrinking during cycling.^{8,9} The study described here focuses on the use of ex-situ AFM to map the hardness of lithium-ion battery cathodes in order to locate the position of the binder material. AFM offers several important advantages over other high-resolution microscopy techniques such as SEM and TEM. For example, AFM studies can be carried out under an ambient atmosphere without the need to dissipate an electron beam current and under experimental conditions that closely resemble the operational environment. Routine AFM imaging with standard probes can resolve sub 100 nm features. The need for electron microscopy techniques to be carried out under high vacuum means that the structure of the material being studied could alter during imaging. The use of energy dispersive analysis by X-rays (EDX, incorporated with most SEMs) for distinguishing between the different electrode components is also not suitable as the spatial resolution is not great enough. This is demonstrated in figure S3 in the supporting information, which shows EDX mapping for fluorine and carbon, the mappings cover the entire image area providing no detail on the spacial distribution of fluorine. The penetration depth of the electron beam may go through multiple active particles, limiting the accuracy since for a purpose such as this, surface sensitivity is important. TEM boasts higher magnifications, up to the atomic scale, but also requires high

vacuum and sample preparation is difficult and may alter the structure of the sample. AFM boasts very good resolution at small scan sizes (down to 1 μm and below) and provides 3D topography of the sample surface. No special sample preparation is required, and the biggest limitation to sample type is roughness (normally only applicable for larger scan sizes). Trivial AFM imaging is also done at ambient temperatures and pressures. With the many different imaging modes available for AFM, most have been applied to battery materials to reveal further insights into their properties and performance as appropriate materials for energy storage devices.¹⁰ Mechanical and conductivity using AFM measurements have excellent spatial resolution as they are only limited by the radius of the tip, which is commonly very small (5-20 nm). Previous studies have used force mapping AFM to image LIB electrodes, most commonly the anode materials, where indentation studies have been used to analyze features such as solid electrolyte interface (SEI).^{11, 12} Even polymer separator materials have been investigated.¹³ Less work has been carried out on cathode materials, probably because there is significantly less surface film growth and surface activity compared to anode materials. Recently, Masuda et al. used bimodal AFM^{14, 15} to measure the Young's modulus across a cross section of a cycled anode and cathode.¹⁶ The images revealed the contrast between the active particles and polymer binder. The present study utilizes nanomechanical mapping and conductive AFM techniques based on an imaging mode called PeakForce Tapping. We have sought to establish proof-of-concept on combined visualization of topographical, electrical and nanomechanical properties of the cathode materials. We demonstrate the ability for these techniques to image both uncycled unmodified commercial cathodes and used materials from an electric vehicle. In doing so we suggest the future perspective of these methods for the detailed study of aging and failure mechanisms in cathode materials. We aim to visualize the location and distribution of the components making up the composite cathodes: active metal oxides, polymer binder and conductive additive. In doing so, the mechanism by which the

composite binds together is determined. This allows us to extract unique insights on the structure of LIB cathode composites that are difficult to obtain by other means, which can contribute to recycling process design. Suggestions about the effect of cycling and aging on the mechanical and conductive properties of the components are also assessed, using a cathode that has been extracted from a used EV.

2.0 Experimental

The materials used for this study are the cathodes from Nissan Leaf pouch cells from two commercial electric vehicle batteries. While the materials are all from the same brand of vehicle, they are from different generations of vehicle and so have different cathode chemistries and structures. The different cathodes are assigned as cathode 1, cathode 2 and cathode 3. Cathode 3 is the same as cathode 2 but taken directly from a used vehicle. Key information about each cell is summarized in table 1.

Table 1. Descriptions of each cell, noting important differences such as cathode chemistry and practical use in a vehicle.	
Cathode	Description
1	Quality control failed material from a 40 kWh vehicle (2 nd generation Nissan Leaf) that has never been assembled into a complete cell. The active material was estimated to be lithium nickel manganese cobalt oxide-532 (LiNiMnCoO ₂ , NMC-532) using EDX analysis (see supporting information). The polymer binder identified as PVDF by the presence of fluorine in the EDX spectrum, and by the melting points observed with differential scanning calorimetry (DSC).

2	Quality control failed material from a 30 kWh vehicle (1 st generation Nissan Leaf), fully assembled into a pouch cell with electrolyte added. The active cathode active material was determined to be a mixture of lithium manganese oxide (LMO) and NMC, this is shown in the supporting information. The ratios cannot be simply determined with EDX alone. For the purposes of this study, the specific ratios are not essential. As with cell A, the polymer binder was also identified as PVDF.
3	Cathode material from a 30 kWh cell (1 st generation Nissan Leaf) removed from a used EV. It is not possible to reliably estimate the active material composition because the cell has been severely aged while being used in the vehicle (roughly 40,000 miles driven). However, it can be assumed it is the same kind of cell as that from which cathode 2 (above) was extracted as both are from a 1 st generation Nissan Leaf.

Cathode 3 was first discharged to 2.7 V (ohmic discharge) before disassembly along with cell B in a glovebox under an atmosphere of argon. The anodes and cathodes from each cell were separated and thoroughly washed with excess dimethyl carbonate (Sigma-Aldrich, anhydrous, $\geq 99\%$) to ensure complete removal of the battery electrolyte. The electrodes were dried in air. Atomic force microscopy (AFM) images and measurements were obtained using a Bruker Dimension Icon AFM, Nanoscope V controller and Nanoscope 9.4 imaging software. PeakForce Tapping (PFT)¹⁷ was the imaging mode utilized for this study. PFT is carried out by oscillating the cantilever at a frequency much lower than its resonance frequency; the probe motion follows a sine wave function. In this mode, the probe contacts the sample until a user-specified setpoint (force) is reached. This generates a force vs time (can be converted to force

vs. tip-sample separation) curve at every pixel in the image (figure 1). This imaging technique allows mechanical properties to be extracted from approach and retract force curves. The modulus (sample hardness) was used to assess the structure of the cathode materials. The chosen model used to calculate the Young's modulus is the Sneddon model,¹⁸ which assumes a conical indenter contacting the sample surface and is fitted from the repulsive region of the retract force curve. For the conductive AFM (C-AFM), PFT was also utilized and the conductivity recorded by measuring the contact current when a 150 mV bias was applied to the samples. The contact current corresponds to the current flow between points B and C on the force vs time curve in figure 1. Scanning electron microscopy was done using a FEI Quanta FEG 650 microscope and EDX analysis was carried out using Aztec software. Scratch tests were carried out using a ST200 scratch tester with a diamond probe and a Zeta-20 3D optical Profiler was used to analyze the scratches. 3 scratches were done on each sample in order to get an average trench depth and a standard deviation.

3.0 Results and Discussion

Commonly, current commercial LIB electrodes are composite coatings on a metal current collector. The coatings contain the active material, a conductive carbon additive and a polymer binder to hold all of the components together and adhere them to the current collector. The amounts of each component in the composite varies between manufacturers, but usually the percentage masses are in the region of: 3-7% binder and 7-10% conductive additive, with the remainder being active material. The materials selected for this study were provided by Nissan as part of a large project focused on battery recycling funded by the UK Faraday Institution (relib.org.uk). Here the strategy was to focus on virgin cathode material and cycled materials from the same manufacturer. Since the cathodes used in this study are from Nissan the composition of the electrodes studied is commercially sensitive, and so the exact composition

is proprietary. Therefore, an assumption has been made that the above percentages are similar across the samples investigated here. The proprietary nature of the materials is a known and experienced issue in the research community. In the world of commercial LIB's, there is a wide range of different chemistries in use, and a wide range of legacy chemistries that are no longer in production. Not being provided with specific details of the materials and chemistries makes commercial cells difficult to study. However, these are the cells that will eventually reach the stage where the materials will need to be recycled in very large quantities, so the need for generic processes that can be applied to most LIB designs and chemistries is critical. This emphasizes the need to study proprietary materials, such as the ones in this study, allowing the development of appropriate recycling techniques.

3.1 Topographical mapping:

We have examined 3 different cathodes from cells that have been defined in the experimental section. Figure 2a) and 2b) shows 5x5 μm AFM topography scans of both cathode 1 and cathode 2, the modulus mapping is shown below each topography image in figure 2c) and 2d). Figure 3 shows a high magnification SEM image of cathode 2, and for comparison the red boxes show the scan sizes of the AFM images used in this study. This emphasizes the advantage that AFM brings with respect to topography detail; adding mechanical properties on top of this makes the technique very powerful. However, SEM is still very useful as a complementary technique due to its ability to provide elemental compositions of the bulk material; this is shown in the supporting information (tables S1, S2 and S3). The detailed morphology of the materials in figure 2 reveals the active material particles for both cathode 1 and cathode 2. The images show a difference in active material particle sizes, with cathode 1 containing smaller active particles ($\sim 0.8\text{-}2\ \mu\text{m}$ diameter) compared to cathode 2 ($\sim 2\text{-}3\ \mu\text{m}$ diameter). The use of differing active particle sizes has been shown to influence cycling behavior, with smaller particle sizes

being favored.^{19, 20} Smaller particles provide shorter path lengths for lithium diffusion and electron transfer, they are also more mechanically forgiving when expanding and contracting during lithium insertion. Thermal stability is also improved with smaller particle sizes in some cases, such as for LiNiO₂ cathodes.²¹

3.2 Modulus mapping:

The modulus mapping for both cathodes shows good contrast across the scanned area, suggesting that the tip is encountering materials of differing hardness. Figures 2 e) and f) show the modulus mapping overlaid onto the 3D topography, demonstrating that the soft areas are not just the low points in the topography, there are some soft areas that are raised up in the 3D image. This shows that the modulus measurements are independent of the topography. Harder areas show a modulus ranging from 150-210 GPa (brighter areas), correlating to the active material particles. Softer areas show a lower modulus of approximately 1 GPa (darker areas), and these are regions where the polymer is located. Previous nanoindentation and AFM indentation studies have shown that PVDF has a modulus of 1-2 GPa, and active material metal oxides have modulus values of as 199 ± 12 GPa and 191 ± 10 GPa for NMC and lithium cobalt oxide (LiCoO₂, LCO) respectively.²²⁻²⁴ It is important to note that the measured modulus values of around 200 GPa are somewhat beyond the quoted accurate limit of instrument in QNM mode. Hence, we take care in interpreting the absolute values with respect to those cited in the literature. In principle the evaluation of Young's modulus requires knowledge of both the applied force per unit area as well as proportional strain in the material being measured. In reality the nano-mechanical methods operated within the AFM cannot determine either of these parameters because the tip contact area is not known and the proportional deformation (strain) cannot be measured. Despite this, standard models for evaluating the Young's modulus from the force-distance curve have been developed on the basis of tip geometry but each of these

has limitations. These models are described in the supportin information. Here we used a conical tip geometry and associated Sneddon model (see experimental section). In order to mitigate any shortcomings in the application of the Sneddon model, the experimental conditions used here were consistently applied in successive measurements and so we are confident that trends can be identified from relative comparisons. Despite this, the values observed in the modulus mappings of figures 2c) and 2d) are within the same order of magnitude as the values reported in literature. It is also worth noting that all the data used in this report were obtained with the same probe and same calibration settings, making the values relative and comparable to each other. The modulus mappings in figure 2 show the ability to distinguish between the components that make up the composite, allowing the PVDF binder to be located, and in turn deduce the way the composite binds together. The softer areas containing the PVDF in cathode 2 in figure 2 d) are located in the gaps between the active particles. The same scenario is also true for cathode 1 in figure 2 c) but the sizes of these gaps are significantly smaller, this is because of the smaller active particles. Figure 4 shows the mechanical mapping on a smaller $2 \times 2 \mu\text{m}$ area, where these particles are seen in more detail. By scanning even smaller, the topography in figure 4 a) and b) reveals agglomerates of small, spherical particles ($\sim 100 \text{ nm}$ in diameter). These are thought to be the conductive carbon additive. Hence these were resolved separately by the use of the conductivity mapping function of the AFM instrument.

3.3 Conductivity mapping:

Conductive AFM (C-AFM) has been used to confirm that these small spherical particles are the conductive additive. Figure 5 shows $2 \times 2 \mu\text{m}$ topography scans (figure 5 a) and b)) with the correlating current mapping (figures 5 c) and d)) for both cathodes. Figures 5 c) and d) show that current flow occurs when the tip is scanned over the agglomerates of small particles

but does not flow when scanned over the larger active material particles (semiconductor metal oxides). The c-AFM images also show that there are different magnitudes of current flowing, mainly evidenced in figure 5 c). This shows that not all agglomerates of conductive additive particles contribute to the conductive network equally. Figure 6 shows a schematic of some possible causes for the differences in conductivity, showing that some conductive particles may be connected to each other all the way down to the current collector, while others may be blocked off by non-conductive active particles. The modulus mapping shows that the softer areas in figures 4 c) and d) coincide with the agglomerates of the small conductive particles, identified by c-AFM and shown in the topography images. The combined QNM and C-AFM suggests that the polymer binder is causing the conductive additive particles to clump together, forming the observed agglomerates, and is likely due to the favorable interactions between the hydrophobic carbon particles and the hydrophobic PVDF polymer. This will aid in providing a secure, well-adhered, conductive network throughout the composite coating. These combined imaging techniques have successfully revealed the binding mechanism of these two composite microstructures: Composite adhesion occurs by the formation of agglomerates of conductive carbon and PVDF that sit in the gaps between the active particles, providing points of contact to multiple active particles and other agglomerates of binder and conductive additive. The effect of active material particle size on the microstructure is also observed. In cathode 2, more PVDF resides between particles, reducing the amount of contact between active particles. This may cause more resistance to lithium diffusion between the active particles. In the case of cathode 1, the smaller active particles can pack together more closely, limiting the volume in-between them, providing higher contact area between particles, improving lithium diffusion. This exposes a balance that needs to be obtained in order to get a strong enough composite, while also maintaining high cell capacity. The voids that form need to be large enough to allow multiple conductive carbon particles to fit in and form these observed agglomerates with the

binder. If the voids are too small to allow this, then the binding mechanism may change. Given the differences in cathode microstructures between manufacturers (and even within the same manufacturer, as is in this case), the need for generic recycling processes with respect to cell design and chemistry is important. Even better would be a standardization in cell design across manufacturers, to enable rapid and efficient dismantling and recycling; currently this does not exist.²⁵

3.4 Cathode ageing:

The effect of cycling and aging can also be evaluated with this technique. Cathode 3 is from a commercial Nissan Leaf EV, one that has been used in the EV for approximately 40,000 miles. Due to the nature of this sample, no detailed information on its cycling/charging/storage/usage history can be obtained. Therefore, an effective evaluation of changes in the microstructure with respect to the cells history cannot be carried out, this is simply a demonstration of the ability of this technique to image such changes. Since we have successfully identified the locations and structures of the binder and conductive carbon additive on the un-cycled materials, the goal of imaging the cycled material would be to observe what happens to these components. How they change will affect the mechanical strength of the composite and so the cell performance will change. Figure 7 a) and b) show 5x5 μm and 2x2 μm topography images respectively of cathode 3. Figures 7 c) and d) show the corresponding modulus maps. It is evident from the images that there has been a change in the morphology of the material, changes in the modulus mapping is also observed. The modulus mapping shows that the maximum modulus had changed from $\sim 150\text{-}210$ GPa to ~ 100 GPa, this suggests the presence of a surface layer that is softer than the active particles. Comparing figure 7 to the images of cathode 2 in figures 2 and 4, the agglomerates of binder and conductive carbon are smaller and do not cover as much of the scanned surface. This shows that with aging, the agglomerates of

binder can be lost, decreasing the mechanical integrity of the composite coating. The loss of these agglomerates could be the result of several factors such as degradation of the binder via chemical/electrochemical means, and/or mechanical disintegration and loss due to active particle swelling and contracting during cycling. The mechanisms of NMC cathode degradation have been the subject of intense study and the effects of micro-mechanical stresses in the active material caused by Li ion intercalation as well as solvent swelling are manifest in macro-scale cracking and loss of active material and transition metal ions. The result of such macro-cracking at the particle/binder interface will necessarily weaken the adhesion of the binder to the particles and form a pathway to the loss of binder from the cathode material consistent with that which we observe here. Our motivation here has been to identify these effects rather than specifically to investigate these mechanisms. Nevertheless, this is an important area of study, understanding how the mechanical structure of the composite changes with aging can aid in developing chemistries and microstructures that are more stable, and systems for material separation for recycling.

3.5 Macro-mechanical testing:

This work has been very effective at evaluation of the microstructure and its mechanical properties at the nanoscale, but recycling processes will ultimately be carried out on the macroscale. In order to correlate the micro-mechanical with the macro-mechanical properties of the electrode materials studied here, we have performed scratch tests on the sample cathodes 2 and 3. This test is not currently commonly used on LIB electrodes but is nevertheless useful in determining not only the adhesion properties of the composite to the current collector, but also the structural integrity of the composite itself. Current techniques include a peel, adhesion and similar scratch-based tests.²⁶⁻²⁸ This test assesses the strength of the composite at a significantly larger scale compare to QNM and so it more appropriate for studying the bulk

material. The method works by dragging a diamond probe across the sample while increasing the load applied to the sample over time. The user defines the load rate and scratch rate. Figures 8 a) and c) shows 3D optical microscope images 10 mm into the scratches on cathodes 2 and 3 respectively. Figures 8 b) and d) show cross sectional plots of the respective scratches. The cross-section plots show that the trench created by the scratch on cathode 2 is $25.86 \pm 1.76 \mu\text{m}$ deep, while that of cathode 3 is $32.78 \pm 0.60 \mu\text{m}$ deep, showing an increase of 22.2 % in the depth of the scratch at the same load. This shows that the cathode 3 composite is not as strong as that of cathode 2, this is due to the various aging phenomena mentioned previously. Therefore, the insights gathered from the QNM data of the used vehicle: that there may be a loss of the agglomerates of conductive carbon and binder, can be linked to the macro-scale scratch test. A loss of such agglomerates would result in weaker contact between active particles and hence a weaker composite overall.

4.0 Conclusion

We have successfully used several AFM modes to distinguish between the multiple components that make up the composite cathode coating from a commercial lithium-ion battery from an EV. PeakForce QNM was used to distinguish between the hard metal oxide active particles and the softer PVDF binder. The combined topography and modulus mapping revealed the binder within agglomerates of small ($\sim 50\text{-}100 \text{ nm}$ diameter) spherical particles, which were confirmed as the conductive carbon additive by using c-AFM. The agglomerates are formed due to the favorable interactions between the hydrophobic PVDF and hydrophobic carbon particles vs the more hydrophilic metal oxide active particles. The effect of cell ageing is addressed and the modulus mapping shows the potential formation of a surface layer and degradation of the polymer agglomerates, leading to a mechanically weaker coating. These

nanomechanical results were linked to the macro-mechanical properties using a scratch test method. This test showed that the aged cathode from a used EV had a weaker composite than the unused cathode, which supports the assessments made using QNM. Techniques such as these can be used for the development of recycling processes by assessing the microstructure of the materials, the information of which can be fed into mechanical treatments to produce pure waste streams.

5.0 Acknowledgements

The authors would like to thank the following people and organizations: The Faraday Institution for funding under project **ReLiB** (<http://relib.org.uk> grant numbers FIRG005 and FIRG006). The electrical power research group, Newcastle University for providing cells 1 and 3. Rob Sommerville, Metallurgy and Materials, University of Birmingham, for providing cell 2. Vishal Panchal, Bruker Nano Surfaces, for constructive advice on the QNM imaging.

6.0 Supporting information available

Supporting material is available related to the analysis of cathode chemistry using a variety of techniques including SEM and EDX elemental mapping as well as thermal characterization using DSC. In addition, the supporting information section contains some relevant background and discussion relating to the quantification of AFM force data using the Peak Force QNM methods. This material is available free of charge via the internet at <https://eur03.safelinks.protection.outlook.com/?url=http%3A%2F%2Fpubs.acs.org%2F&data=02%7C01%7Cksr7%40leicester.ac.uk%7Ce31971842cc8433c59a508d7fdbd507c%7Caebeed6a31d44b0195ce8274afe853d9%7C0%7C0%7C637256861851165075&sdata=oP4bCyATvMN93LM15iT99h%2Bwh0XshhKqGBCdMCMnWUA%3D&reserved=0>.

7.0 References

- [1] Peled, E. The Electrochemical Behavior of Alkali and Alkaline Earth Metals in Nonaqueous Battery Systems-The Solid Electrolyte Interphase Model. *J. Electrochem Soc.* **2006**, *126*, 2047.
- [2] Peled, E.; Menkin, S. Review-SEI: Past, Present and Future. *J. Electrochem Soc.* **2017**, *164*, 1703-1719.
- [3] Peled, E.; Golodnitsky, D.; Penciner, J. The Handbook of Battery Materials 2nd Edition, John Wiley & Sons Ltd, **2011**, 479-523.
- [4] Zhan, C.; Wu, T.; Lu, J.; Amine, K. Dissolution, migration and deposition of transition metal ions in Li-ion batteries exemplified by Mn-based cathodes – a critical review. *Energy Environ. Sci.* **2018**, *11*, 243-257.
- [5] Gilbert, J. A.; Shkrob, I. A.; Abraham, D.P. Transition Metal Dissolution, Ion Migration, Electrocatalytic Reduction and Capacity Loss in Lithium-Ion Fuel Cells. *J. Electrochem Soc.* **2017**, *164*, 389-399.
- [6] Chen, D.; Indris, S.; Schulz, M.; Gamer, B.; Mönig, R. In situ Scanning Electron Microscopy on Lithium Ion Battery Electrodes Using an Ionic Liquid. *J. Power Sources* **2011**, *1*, 6382-6387.
- [7] Huang, J. Y.; Zhong, L.; Wang, C. M.; Sullivan, J. P.; Xu, W.; Zhang, L. Q.; Mao, S. X.; Hudak, N. S.; Liu, X. H.; Subramanian, A.; Fan, H.; Qi, L.; Kushima, A. In situ Observation of the Electrochemical Lithiation of a Single SnO₂ Nanowire Electrode. *Science* **2010**, *330*, 1515-1519.

- [8] Ramdon, S.; Bhushan, B.; Nagpure, S. C. In situ Electrochemical Studies of Lithium-Ion Battery Cathodes Using Atomic Force Microscopy. *J. Power Sources* **2014**, *249*, 373-384.
- [9] Demirocak, D. E; Bhushan, B. In situ Atomic Force Microscopy Analysis of Morphology and Particle Size Changes in Lithium Iron Phosphate Cathode During Discharge. *J. Colloid. Interface Sci.* **2014**, *423*, 151-157.
- [10] Kempaiah, R.; Vasudevamurthy, G.; Subramanian, A. Scanning Probe Microscopy Based Characterization of Battery Materials, Interfaces and Processes. *Nano Energy* **2019**, *65*, 103925-103959.
- [11] Kumar, R.; Tokranov, A.; Sheldon, B. W.; Xiao, X.; Huang, Z.; Li, C.; Mueller, T. In situ and Operando Investigations of Failure Mechanisms of the Solid Electrolyte Interphase on Silicon Electrodes. *ACS Energy Lett.* **2016**, *1*, 689-697,
- [12] Liu, X.R.; Deng, X.; Liu, R. R.; Yan, H. J.; Guo, Y. G.; Wang, D. Single Nanowire Electrode Electrochemistry of Silicon Anode by in situ Atomic Force Microscopy: Solid Electrolyte Interphase Growth and Mechanical Properties. *ACS Appl. Mater. Interfaces* **2014**, *6*, 20317-20323.
- [13] Chen, J.; Yan, Y.; Sun, T.; Qi, Y.; Li, X. Deformation and Fracture Behaviors of Microporous Polymer Separators of Lithium Ion Batteries. *RSC Adv.* **2014**, *4*, 14904-14914.
- [14] Labuda, A.; Kocun, M.; Meinhold, W.; Walters, D.; Proksch, R. Generalized Hertz Model for Bimodal Nanomechanical Mapping. *J. Nanotechnol.* **2016**, *7*, 970-982.
- [15] Labuda, A.; Kocum, M.; Meinhold, W.; Revenko, I.; Proksch, R. Fast, High Resolution, and Wide Modulus Range nanomechanical Mapping with Bimodal Tapping Mode. *ACS Nano*. **2017**, *11*, 10097-10105.

- [16] Sakai, H.; Taniguchi, Y.; Uosaki, K.; Masuda, K. Quantitative Cross-Sectional Mapping of Nanomechanical Properties of Composite Films for Lithium Ion Batteries Using Bimodal Mode Atomic Force Microscopy. *J. Power Sources* **2019**, *413*, 29-33.
- [17] Xu, K.; Sun, W.; Shao, Y.; Wei, F.; Zhang, X.; Wang, W. Recent Development of PeakForce Tapping Mode Atomic Force Microscopy and its Applications on Nanoscience. *Nanotechnol. Rev.* **2018**, *7*, 605-621.
- [18] Sneddon, I. N. The Relation Between Load and Penetration in the Axisymmetric Boussinesq Problem for a Punch of Arbitrary Profile. *Int. J. Eng. Sci.* **1965**, *3*, 47-57.
- [19] Sheu, S. P.; Yao, C. Y.; Chen, J. M.; Chiou, Y. C. Influence of the LiCoO₂ Particle Size on the Performance of Lithium-Ion Batteries, *J. Power Sources* **1997**, *68*, 533-535.
- [20] Sinha, N. N.; Munichandraiah, N. The Effect of Particle Size on Performance of Cathode Materials of Li-ion Batteries. *J. Indian Institute of Science* **2009**, *89*, 381-392.
- [21] Hwang, I.; Lee, C. W.; Kim, J. C.; Yoon, S. Particle Size Effect of Ni-rich Cathode Materials on Lithium Ion Battery Performance. *Mater. Res. Bull.* **2012**, *47*, 73-78.
- [22] Nguyen, Q. D.; Oh, E. S.; Chung, K. H. Nanomechanical Properties of Polymer Binders for Li-ion Batteries Probed with Colloidal Probe Atomic Force Microscopy. *Polym. Test.* **2019**, *76*, 245-253.
- [23] Cheng, E. J.; Taylor, N. J.; Wolfenstine, J.; Sakamoto, J. Elastic Properties of Lithium Cobalt Oxide (LiCoO₂). *J. Asian ceram. Soc.* **2017**, *5*, 113-117.
- [24] Cheng, E. J.; Hong, K.; Taylor, N. J.; Choe, H.; Wolfenstine, J.; Sakamoto, J. Mechanical and Physical Properties of LiNi_{0.33}Mn_{0.33}Co_{0.33}O₂ (NMC), *J. Eur. Ceram. Soc.* **2017**, *37*, 3213-3217.
- [25] Harper, G.; Sommerville, R.; Kendrick, E.; Driscoll, L.; Slater, P.; Stolkin, R.; Walton, A.; Christensen, P.; Heidrich, O.; Lambert, S.; Abbott, A.; Ryder, K.; Gains, L.;

- Anderson, P. Recycling Lithium-Ion Batteries From Electric Vehicles. *Nature* **2019**, *575*, 75-86.
- [26] Luo, H.; Sahraei, E.; Xia, Y. Adhesion Strength of the Cathode in Lithium-ion Batteries Under Combined Tension/Shear Loadings. *RSC Adv.* **2018**, *8*, 3996-4005.
- [27] Haselrieder, W.; Westphal, D.; Bockholt, H.; Diener, A.; Höft, S.; Kwade, A. Measuring the Coating Adhesion Strength of Electrodes for Lithium-ion Batteries. *Int. J. Adhes. Adhes.* **2015**, *60*, 1-8.
- [28] Son, B.; Ryou, M. H.; Choi, J.; Lee, T.; Yu, H.K.; Kim, J. H. Measurement and Analysis of Adhesion Property of Lithium-Ion Battery Electrodes with SAICAS. *ACS Appl. Mater. Interfaces* **2014**, *6*, 526-531.

Figures:

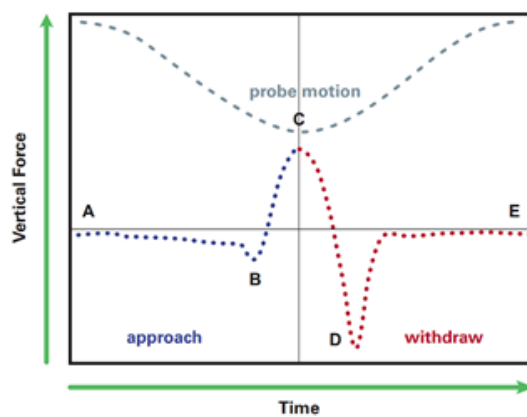


Figure 1. Schematic of a force vs. time plot demonstrating the AFM probe motion during peak force tapping mode and the resulting force response due to tip-sample interactions.

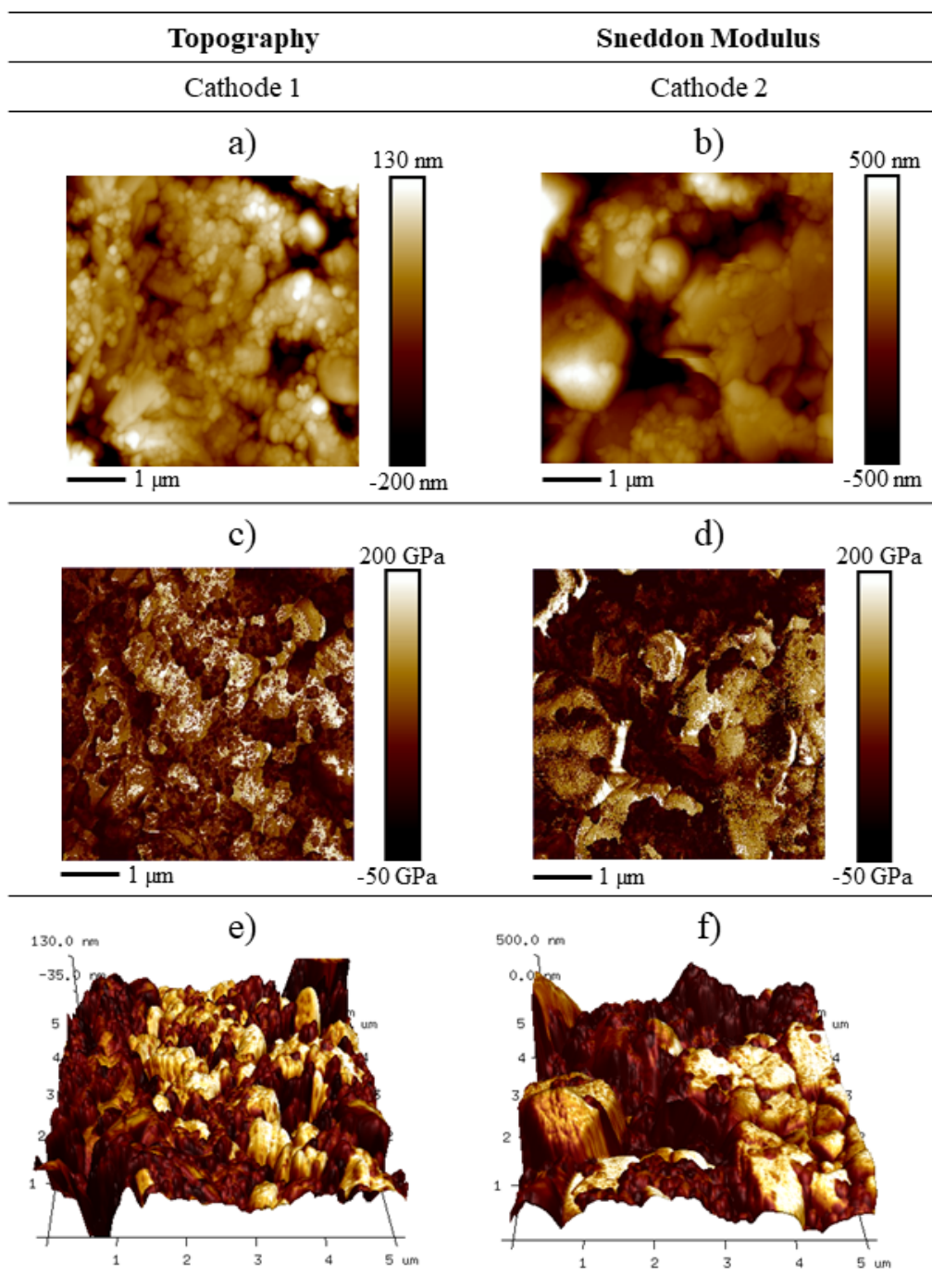


Figure 2. 5x5 μm AFM topography images and corresponding modulus mapping of cathodes from two different commercial cells. a) and b): topography for cathodes 1 and 2 respectively. c) and d) modulus map for cathodes 1 and 2 respectively. e) and f) show the modulus maps overlaid onto the 3D topography for cathodes 1 and 2 respectively. Images recorded using a Bruker RTESPA-525 probe, a setpoint of 400 nN and a peak force amplitude of 300 nm.

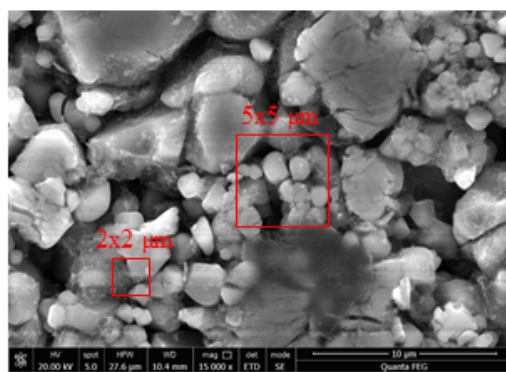


Figure 3. SEM image of cathode 2 at 15,000x magnification. The red boxes drawn on represent the AFM scan sizes used in this study. The much smaller scan sizes show that much more detailed topography information can be obtained very easily with AFM.

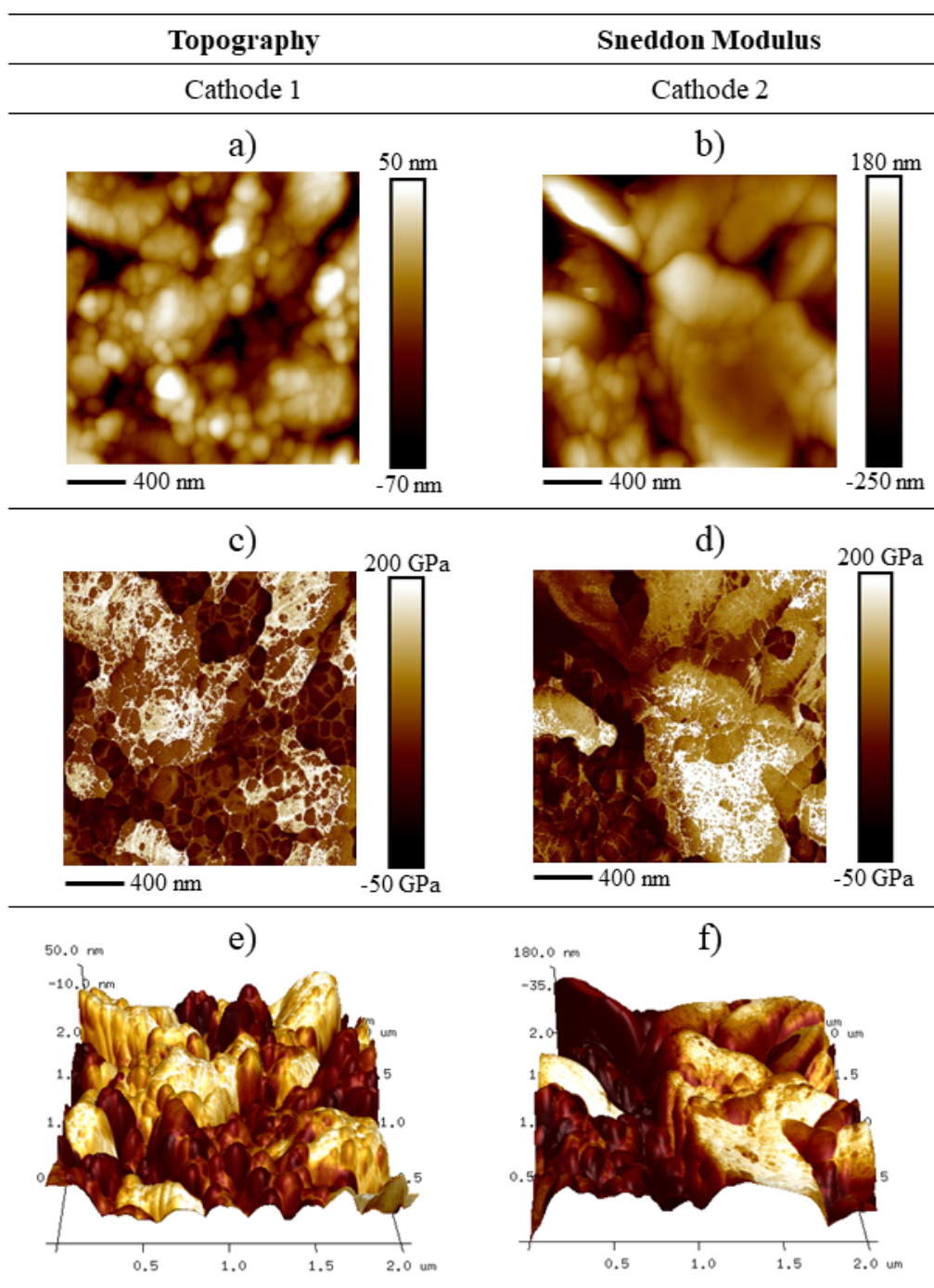


Figure 4. 2x2 μm AFM topography images and corresponding modulus mapping of cathodes from two different commercial cells. a) and b): topography for cathodes 1 and 2 respectively. c) and d) modulus map for cathodes 1 and 2 respectively. e) and f) show the modulus maps overlaid onto the 3D topography for cathodes 1 and 2 respectively. Images recorded using a Bruker RTESPA-525 probe, a setpoint of 400 nN and a peak force amplitude of 300 nm.

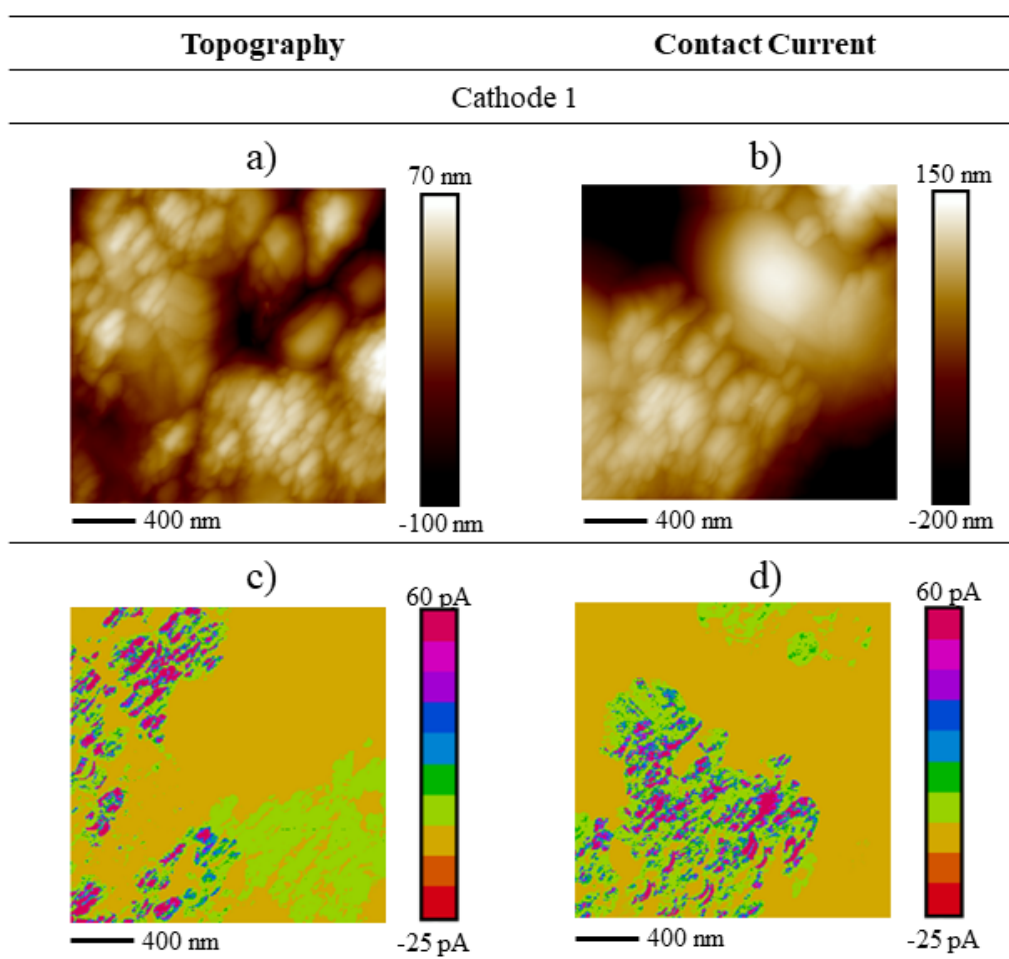


Figure 5. 2x2 μm topography and conductivity mapping, showing contact current, of cathode 1: a) and c), and cathode 2: b) and d). The images were recorded using an AD-40-AS boron doped diamond probe from Adama Innovations. A voltage bias of 150 mV was applied to the sample.

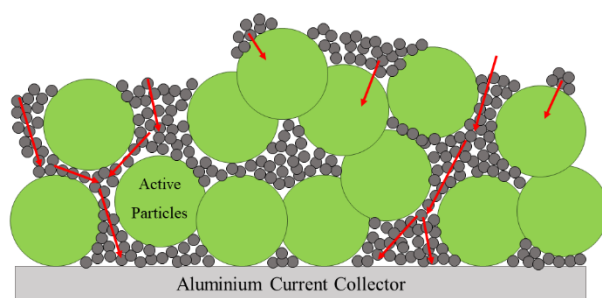


Figure 6. Schematic showing the potential paths for electrical conductivity through the composite coating. The image shows some particles connecting all the way to the current collector, while some are blocked by the active particles.

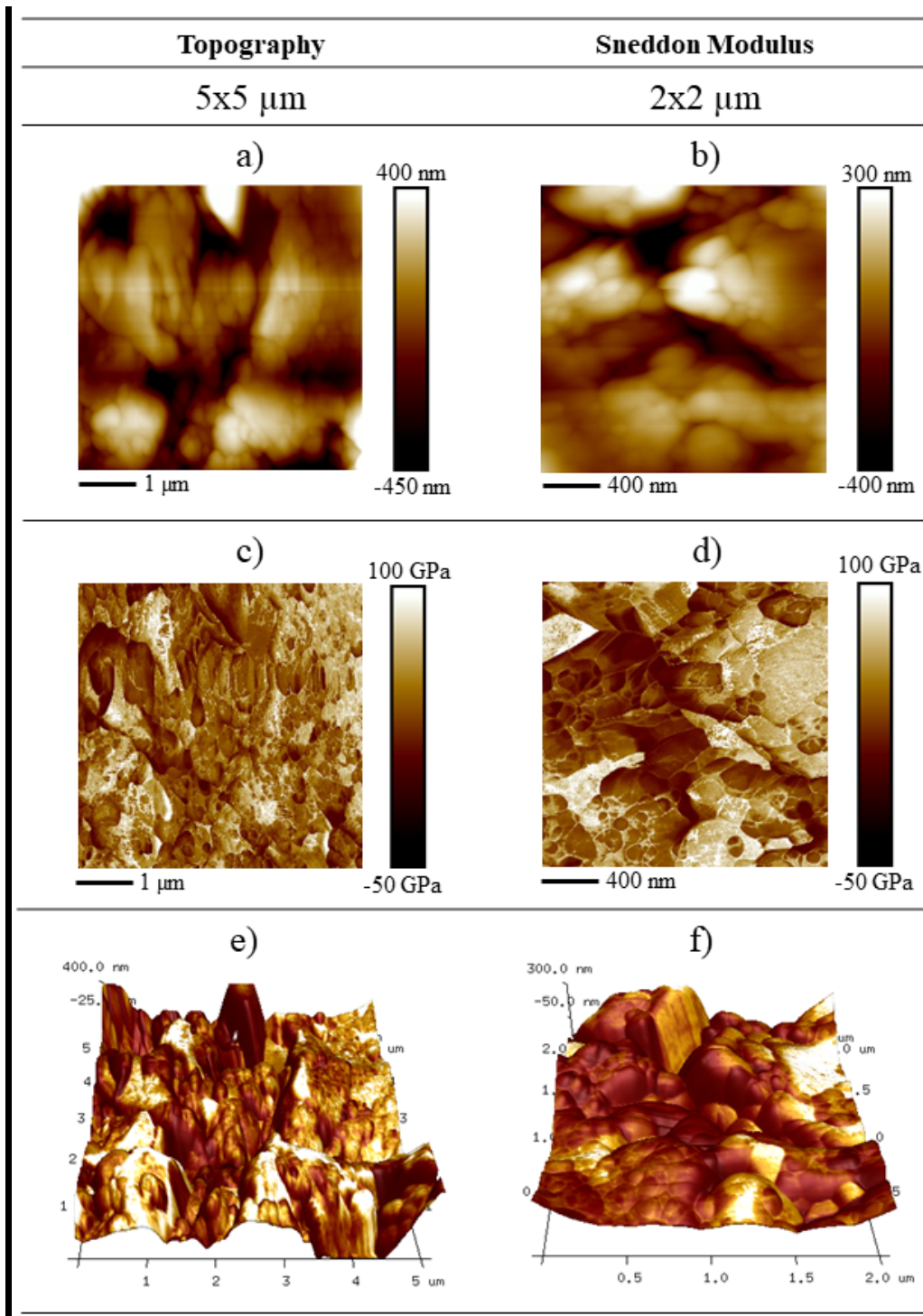


Figure 7. 5x5 μm and 2x2 μm AFM topography images, a) and b) respectively, and corresponding modulus mapping, c and d), of cathodes from a used electric vehicle. Images e) and f) show the modulus overlaid onto the 3D topography. Images recorded using a Bruker RTESPA-525 probe, a setpoint of 400 nN and a peak force amplitude of 300 nm.

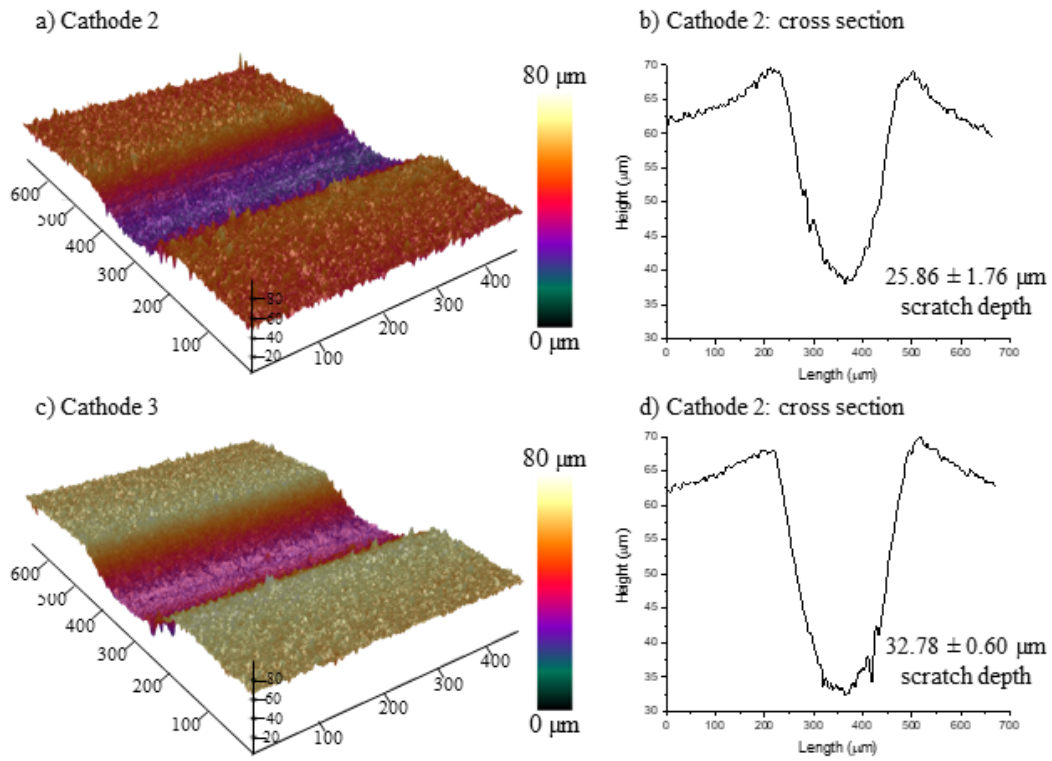


Figure 8. 3D optical microscope images 10 mm into the scratch of a) cathode 2 and c) cathode 3. Cross sections of cathode 2 and cathode 3 are shown in b) and d) respectively, showing the depth of the scratch and the standard deviation from 3 scratches. Parameters used for the scratch were 1 N initial load, 10 N final load, 40 N min⁻¹ load rate and 200 mm min⁻¹ table rate. The load on the cathodes at 10 mm is 3 N. The tests show that at the same point in the scratch, the depth is 21.2% greater for the aged cathode.

TOC Graphic

